

See discussions, stats, and author profiles for this publication at: <https://www.researchgate.net/publication/229309191>

Dynamics of exciplex formation in rare gas media

ARTICLE *in* CHEMICAL PHYSICS · JULY 2009

Impact Factor: 1.65 · DOI: 10.1016/j.chemphys.2009.06.002

CITATIONS

4

READS

23

3 AUTHORS, INCLUDING:



[Germán Rojas-Lorenzo](#)

Instituto Superior de Tecnologías y Ciencia...

32 PUBLICATIONS 273 CITATIONS

[SEE PROFILE](#)



[Jesus Rubayo-Soneira](#)

Instituto Superior de Tecnologías y Ciencia...

68 PUBLICATIONS 659 CITATIONS

[SEE PROFILE](#)



Dynamics of exciplex formation in rare gas media

Germán Rojas-Lorenzo^{a,b,*}, Jesús Rubayo-Soneira^a, Sebastián Fernández Alberti^c

^a Departamento de Física General y Matemáticas, Instituto Superior de Tecnologías y Ciencias Aplicadas, La Habana, Cuba

^b Instituto de Física Fundamental, Consejo Superior de Investigaciones Científicas, Serrano 123, 28006 Madrid, Spain

^c Centro de Estudios e Investigaciones, Universidad Nacional de Quilmes, Roque Sáenz Peña 180, Bernal B1876BXD, Argentina

ARTICLE INFO

Article history:

Received 16 March 2009

Accepted 3 June 2009

Available online 6 June 2009

Keywords:

Rare gas matrices

Photoinduced molecular complex formation

Molecular dynamics

Non-adiabatic couplings

Hopping surface

ABSTRACT

A hopping-surface algorithm has been used to simulate the dynamics induced in rare gas matrices due to the photoexcitation ($^1S_0 \rightarrow ^3P_1$) of atomic mercury embedded in them. Especially, the study of the dynamics of an exciplex formation in a model system consisting of solid xenon doped with atomic mercury. The process starts upon the photoexcitation of the Hg atom to its 3P_1 electronic excited state. Diatomics-in-Molecule approach has been used for constructing the adiabatic potential surfaces. In all trajectories we show that a triatomic Xe–Hg⁺–Xe complex is formed, but in two conformations: bent and linear. The mechanisms leading to the formation of one or the other are identified. Mainly, are noted the thermal fluctuations of the Hg impurity and the shape of the potential surfaces. Furthermore, we show that non-radiative intrastate relaxation occurs via a conical intersection between the excited state surfaces. The simulated spectra are in very good agreement with the experimental data.

© 2009 Elsevier B.V. All rights reserved.

1. Introduction

In many non-metallic solids, severe local lattice rearrangements are induced by excitation of either bulk or defect electronic states with strong electron-phonon coupling. This leads to formation of atomic- or molecular-type defects in metal halides [1–3] and oxides [4,5], in van der Waals solids [6–9], in polymer films [10], in low dimensional solids [11,12], and in doped glasses [13,14]. Defect formation is also a precursor of the desorption and sputtering from surfaces and of the radiation damage in solids.

Photoinduced defect formation has been investigated by a wide variety of conventional and ultrafast spectroscopic techniques. Nevertheless, the molecular structure of such defects and the mechanisms leading to their formation, have remained largely unknown, due to the lack of adequate experimental observables. Although ultrafast spectroscopy manages to capture the dynamics of defect formation in “real-time” [1–3,7,9,11,12], it does not provide the structural details, which can only be retrieved using simple models based on effective coordinates. The full description of the dynamics of defect formation requires knowledge of the potential surfaces and the non-adiabatic couplings that mediate the process. Here, we present a simulation study of a model system consisting of an Hg impurity embedded in rare gas (Rg) solids Ne, Ar, Kr, and Xe, which contains features of photoinduced atomic

or molecular defect formation, common to a large class of systems [1–3,7–10,15]. Excitation of the 3P_1 state of Hg in solid Xe leads to a strongly Stokes-shifted (by $\sim 3000\text{ cm}^{-1}$) and broadened emission [16,17], which has been attributed to the formation of an excited complex Hg–Xe [16]. This is in stark contrast with Hg in lighter rare gas solids, which exhibit a small Stokes shift ($\sim 800\text{ cm}^{-1}$), suggesting little lattice rearrangement around the impurity, which therefore retains its atomic character [16–19].

In order to simulate the dynamics, and in the especial case of Xe matrices leading to complex formation, we use the Molecular Dynamics with Quantum Transitions (MDQT) algorithm [20,21], which treats the electronic degrees of freedom quantum mechanically, while nuclear motions are treated classically.

2. The MDQT method

Briefly, the MDQT method treats the electronic degrees of freedom quantum mechanically, while the motions of the nuclei are treated classically. The nuclei evolve on a PES that is defined by a single electronic state at a given time. Hops from one electronic state to another are governed by the coefficients of the electronic wave function.

In the present work the electronic wave function is written as:

$$\psi(r, R, t) = \sum_i c_i(t) \phi_i(r; R), \quad (1)$$

where r and R are the electronic and nuclear coordinates, respectively. $\phi_i(r; R)$ is the eigenstate of the electronic Hamiltonian $H^{\text{Hg-Rg}}$ with energy $E_i(R)$,

* Corresponding author. Address: Departamento de Física General y Matemáticas, Instituto Superior de Tecnologías y Ciencias Aplicadas, La Habana, Cuba. Tel.: +53 7 8789858.

E-mail address: grojas37@gmail.com (G. Rojas-Lorenzo).

$$H^{\text{Hg-Rg}}(r; R)\phi_i(r; R) = E_i(R)\phi_i(r; R). \quad (2)$$

The coefficients $c_i(t)$ evolve in time according to

$$i\hbar\dot{c}_i(t) = c_i(t)E_i - i\hbar \sum_j c_j(t)\hat{\mathbf{R}}\mathbf{d}_{ij}, \quad (3)$$

where

$$\mathbf{d}_{ij} = \langle \phi_i(r; R) | \nabla_R \phi_j(r; R) \rangle, \quad (4)$$

is the non-adiabatic coupling vector.

3. Potential energy surfaces and couplings

The ^3P state of mercury splits into two states in the linear Rg–Hg complex: $^3\Pi$ and $^3\Sigma$ differing by the projection of the excited orbital onto the interatomic axis and by their bonding energies. The further mixing due to the spin-orbit coupling gives rise to the $A|0^+\rangle = |^3\Pi\rangle$ and the $B|1\rangle = (|^3\Pi\rangle + |^3\Sigma\rangle)/2$ stationary states. The A -state is allocated to the $|J=1, \Omega=0\rangle$ electronic state associated to the projection $\Omega=0$ of the mercury electronic angular momentum $J=1$ onto the interatomic axis. Correspondingly, the B -state is allocated to the $|J=1, \Omega=\pm 1\rangle$ state of the complex. Their potential curves $V_A(R)$ and $V_B(R)$ have been deduced experimentally [22–24] and are represented by the Morse pair potentials along with ground state potential V_X . The potential parameters [22–25] we used are given in the Table 1. The Rg–Rg interactions are described by the Lennard Jones pair potentials. Using the J, Ω basis seems more realistic because of the important spin-orbit coupling in Hg–Rg.

The total interaction Hamiltonian, $H^{\text{Hg-Rg}}$, for the ground electronic state correlating asymptotically to $\text{Hg}(^1\text{S}_0)$ is written simply as the sum of pairwise interactions. However, as already mentioned this cannot be applied to the excited states involving an electronic angular momentum different from zero (e.g., $\text{Hg}(^3\text{P}_1)$) where the quantization axis cannot be defined simultaneously along each Hg–Ar bond. To this end, we follow the model proposed by Zuniga et al. [26]: by $|J, \Omega\rangle_Z$ we denote the electronic wave functions of the mercury atom with projection Ω on axis Z and by $|J, \Omega\rangle_{Z_k}$ the corresponding wave function with projection Ω on the $\text{Hg} \cdots \text{Rg}_k$ axis. The transformation

$$|J, \Omega\rangle_Z = \sum_{\Omega'} D_{\Omega\Omega'}^J(\phi_k, \theta_k, 0) |J, \Omega'\rangle_{Z_k}, \quad (5)$$

$D_{\Omega\Omega'}^J(\phi_k, \theta_k, 0)$ is the Wigner rotation matrix, θ_k and ϕ_k the polar angles that define the orientation of the particular $\text{Hg} \cdots \text{Rg}$ with re-

spect to axis Z . The matrix elements of the $\text{Hg} \cdots \text{Rg}_k$ diatomic Hamiltonian $H^{\text{Hg-Rg}_k}$ in the $|J, \Omega\rangle_Z$ representation is written as

$$\langle J, \Omega' | H^{\text{Hg-Rg}_k} | J, \Omega'' \rangle_Z = \sum_{\Omega} D_{\Omega'\Omega}^J(\phi_k, \theta_k, 0) D_{\Omega''\Omega}^J(\phi_k, \theta_k, 0) V_{\Omega}(R_k), \quad (6)$$

where

$$V_{\Omega}(R_k) = \langle J, \Omega | H^{\text{Hg-Rg}_k} | J, \Omega \rangle_{Z_k} \quad (7)$$

are the potentials denoted as V_A and V_B .

This procedure is repeated for each $\text{Hg} \cdots \text{Rg}$ bond in the whole system, leading to non-diagonal elements in the total electronic Hamiltonian of the system. The total electrostatic interaction Hamiltonian of Hg atom with n_{Rg} rare gas atoms in the solid is written as:

$$H^{\text{Hg-Rg}} = \sum_{k=1}^{n_{\text{Rg}}} H^{\text{Hg-Rg}_k} \quad (8)$$

We then diagonalise the resulting *diabatic* matrix of $H^{\text{Hg-Rg}}$ in order to obtain the *adiabatic* energies E_i of Eq. (2). The practical implementation of this procedure is given in the Appendix of Ref. [27]. The resulting potential curves for the different matrices are shown in Fig. 2. Using the J, Ω basis seems more realistic because of the important spin-orbit coupling in Hg–Rg.

4. Molecular dynamics simulations

The calculations described in this work were carried out with minimum image convention for a system composed of 1 Hg atom and 499 Rg atoms. The number of Rg atoms corresponds to a box large enough to avoid size effects, at least at the short timescales of the dynamical simulations. The Hg atom was initially placed at a monosubstitutional site of the rare gas matrix. We only explored the monosubstitutional site according to previous experimental and theoretical reports [19,27]. No other sites in the matrix were explored.

As the first step in our calculations, the system was equilibrated in the electronic ground state for 400 ps at an effective temperature T . The last 200 ps were used to collect a set of initial positions and momenta for the subsequent simulations in the excited states. The stored configurations fulfil the classical Franck principle for the electronic transition from the ground state to one of the three possible adiabatic excited states defined by Eq. (2) and asymptotically correlated to $\text{Hg}(^3\text{P}_1)$. At this energy, each excitation event is found to reach one of these states. In fact, the population produced in the three states by all the excitation events remains constant.

One hundred trajectories of 10 ps each were run from these initial configurations by Franck–Condon switching to each of the three excited states. The propagation time was sufficient to achieve a convergence of the final electronic state populations in time. In order to represent the vibrational amplitudes of the Rg atoms we adjusted their velocities to an effective temperature T' estimated with the procedure described in Ref. [28].

The trajectories were run at the effective constant temperatures of 17 K, 49 K, 36 K and 32 K for Ne, Ar, Kr, and Xe matrices, respectively. These temperatures are chosen in such a way that the classical probability distribution for the atomic rare gas motions at T' equals the quantum probability distribution at the actual experimental temperature of 4 K. Debye frequencies of solid Ne ($\omega = 55 \text{ cm}^{-1}$), Ar ($\omega = 66 \text{ cm}^{-1}$), Kr ($\omega = 50 \text{ cm}^{-1}$) and Xe ($\omega = 43 \text{ cm}^{-1}$) were considered.

5. Spectroscopy of Hg in rare gas matrices

The lowest excited states of Hg consists of the $^3\text{P}_0$, $^3\text{P}_1$ and $^3\text{P}_2$ levels in order of ascending energy, which are separated by several

Table 1

Potential energy of Hg–Rg for the ground state and the A and B excited states, denoted by V_X , V_A and V_B , respectively [22–26].

	$D_0 \text{ (cm}^{-1}\text{)}$	$\beta \text{ (\AA}^{-1}\text{)}$	$r_e \text{ (\AA)}$
Ne–Hg(X) [22]	37	1.586	3.90
Ne–Hg(A) [22]	70	1.764	3.47
Ne–Hg(B) [22]	11	1.242	4.92
Ar–Hg(X) [26]	130	1.448	3.98
Ar–Hg(A) [26]	354	1.541	3.34
Ar–Hg(B) [26]	52	1.116	4.66
Kr–Hg(X) [23]	178	1.405	4.07
Kr–Hg(A) [23]	629	1.519	3.35
Kr–Hg(B) [23]	105	1.017	4.58
Xe–Hg(X) [24]	245	1.268	4.25
Xe–Hg(A) [24]	1417	2.305	3.25
Xe–Hg(B) [24]	167	0.864	4.47
	$\varepsilon \text{ (cm}^{-1}\text{)}$	$\sigma \text{ (\AA)}$	
Ne–Ne [25]	25	2.74	
Ar–Ar [25]	84	3.40	
Kr–Kr [25]	113	3.65	
Xe–Xe [25]	161	3.98	

Table 2

Calculated and Experimental(*) [16–18] values of spectroscopic properties for the mercury electronic transition $^1S_0 \leftrightarrow ^3P_1$. In the table Abs. and Ems. represent the values at the maxima in absorption and emission bands, respectively, σ is the FWHM, and SShift denotes Stokes shift. All values are reported in cm^{-1} .

	Abs.	σ_a	Ems.	σ_e	SShift
Ne	40397	449	39454	264	943
	40404*	400*	39604*	400*	800*
Ar	40689	560	39981	480	697
	40650*	430*	39940*	400*	710*
Kr	40150	361	39415	457	735
	40150*	340*	39350*	420*	800*
Xe	39361	163	36169	1289	3192
	39400*	330*	36500*	1200*	2900*

thousands of cm^{-1} . Only the 3P_1 level is accessible by absorption from the ground state, both in the gas phase and in matrices. The energies at band maxima, absorption–emission Stokes shifts, and bandwidths from the experiment and the present work are compared in Table 2. Clearly, the simulations qualitatively reproduce the experimental data. A relative blue shift of the absorption spectra is observed while moving from krypton to Neon and Argon matrices. Moreover, the triplet fine structure of the absorption spectrum in Xe matrix has been reproduced, see Fig. 1. The absorption spectrum consists of transitions from the ground state to the three degenerate diabatic states ($J = 1$, $\Omega = 0, \pm 1$). Therefore, it can be decomposed in three subbands, which is due to the degeneracy of the 3P_1 states. This fact, shows that it is not due to a dynamical John–Teller effect as it was claimed based on the analysis of MCD spectra [29–31].

While the emission energies (Table 1) for the $\text{Hg}(^1S_0 \rightarrow ^3P_1)$ transition in Ne and Ar matrices present a blue shift compared to gas phase (39412 cm^{-1}), a slightly red shifted is observed in Kr. Despite

that, the emission bands have comparable FWHM in these three matrices. On the other hand, differential features can be remarked for the emission of the $\text{Hg}(^1S_0 \rightarrow ^3P_1)$ transition in xenon matrix. A strong red shifted with respect to the gas phase is observed and its bandwidth is typically three times larger than in the other matrices. Moreover, in addition to the $^3P_1 \rightarrow ^1S_0$ emission, excitation of the 3P_1 level also gives rise to emission of the lower lying (by 1765 cm^{-1} in the gas phase) 3P_0 , that is long-lived due to the dipole-forbidden character of its transition to the ground state. This indicates the presence of $^3P_1 \rightarrow ^3P_0$ intramultiplet non-radiative relaxation following pulsed laser excitation of the 3P_1 level.

More important in the context of the structural dynamics are the Stokes shifts, which are also well reproduced by the simulation, both in trend and in magnitude, within 8% for Ne/Hg, Ar/Hg and Kr/Hg. For Xe/Hg matrices, the values agree less well (within 20%), which however is not too surprising given the approximations made in the method we adopted, the quality of pair potentials and the extent of the structural rearrangement process.

The steady-state absorption and emission bands represent the initial and final stages of the photoinduced structural rearrangement process around excited Hg. The fact that these features are reasonably well reproduced by the simulation ensures us that the molecular dynamics that interpolates these two ends reflects the actual rearrangement processes occurring in the system. In the case of Ne/Hg and Kr/Hg matrices, the relaxation is quite similar to what we already reported in the case of Ar/Hg matrices [27] and we will briefly review the results for all three matrices. On the contrary, a wholly different mechanism takes place in Xe/Hg matrices, which is the main result of this contribution.

6. Electronic representations in Rg/Hg matrices

The MDQT method was used in the adiabatic representation of the excited electronic states, i.e., the nuclei move on adiabatic po-

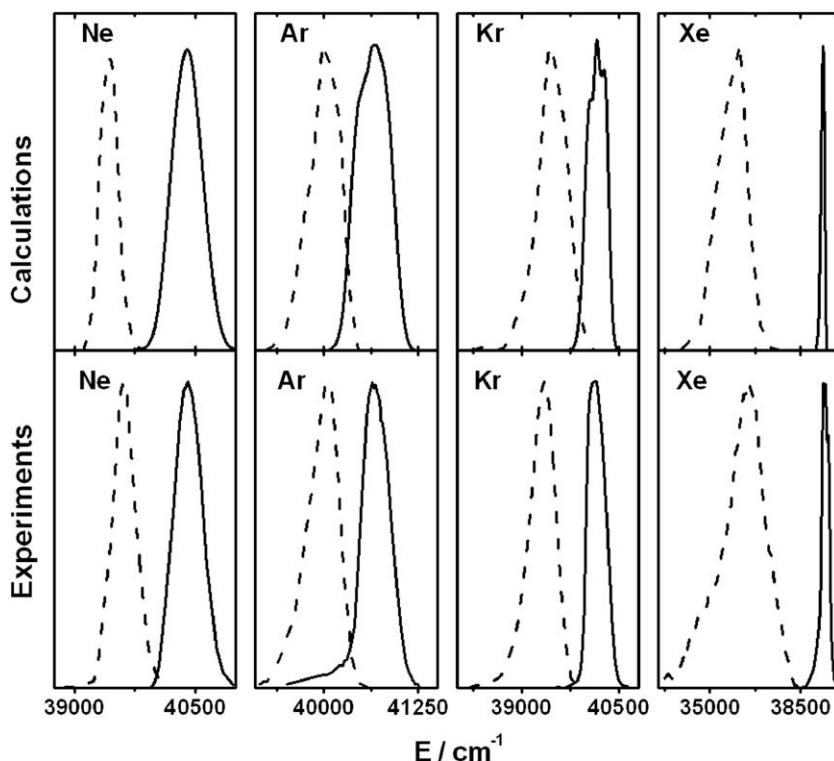


Fig. 1. Experimental and simulated spectra for the $\text{Hg}(^1S_0 \rightarrow ^3P_1)$ transition in rare gas matrices. Solid lines represent absorption bands ($^1S_0 \rightarrow ^3P_1$), and dashed lines represent emission bands ($^3P_1 \rightarrow ^1S_0$).

tential energy surfaces. Nevertheless, the description in terms of *adiabatic states*, which are defined in the diatomic frame as the $|J=1, \Omega=0\rangle$, $|J=1, \Omega=+1\rangle$, and $|J=1, \Omega=-1\rangle$ states, is however still valid in the matrix. As we have previously reported for the case of Hg/Ar [27], the populations of these three diabatic states fluctuates close to $\sim 33\%$ during the dynamics in all the studied systems (Rg/Hg, Rg = Ne, Ar, Kr, and Xe). This situation is due to the temporal behaviour of diabatic couplings among these states. These diabatic couplings increase from the beginning reaching their maximum values in 1–2 ps of dynamics. Thereafter, the couplings remain oscillating in time up to the end of the simulation. As a consequence, the transfer of population is favoured among the states during all the dynamics. Since the three diabatic levels are populated at the end of the dynamics, all of them contribute to the triplet emission band. However, a single structure [27] is observed in the experiments. This is in coincidence with the results of our simulations analyzed in terms of the electronic adiabatic representation. In this case, the level with less energy (adiabatic level 1) is populated up to 100% in all the Rg matrices before 1.5 ps of molecular dynamics. Therefore, the emission takes place only from this adiabatic state and the emission band has a single structure as in the experiments. In agreement with our previous report in Ar matrices [27], the adiabatic couplings among the levels are strong at the beginning of the process but they rapidly decrease almost to zero, remaining negligible during the rest of the simulations [27]. Differences among the dynamics in the Rg matrices are mainly localized in the time interval needed to populate the adiabatic level 1 up to 100%. As is shown in Fig. 3 this time interval changes in the different matrices being the longest for Xe matrices.

The energy gap among the adiabatic electronic states reached by the system after the photoexcitation of the Hg impurity to its 3P_1 electronic excited state, are smaller in the argon and the krypton matrices than in the neon and the xenon matrices (Fig. 2). As a consequence, the transfer of electronic population among the states is faster in Ar/Hg and Kr/Hg matrices than in Ne/Hg and Xe/Hg solids. It is worth to mention that the \tilde{a} -state, correlated to the mercury atomic level 3P_0 , has been kept unpopulated during the time of our simulations. Previous studies have shown that the efficiency of the intramultiplet relaxation is 1:200.

7. Structural dynamics in Ne, Ar and Kr solids

For Ne/Hg, Ar/Hg and Kr/Hg matrices, the absorption–emission Stokes shifts are comparable. As it was shown for the case of Ar matrices [27] the structural relaxation corresponds to a slight

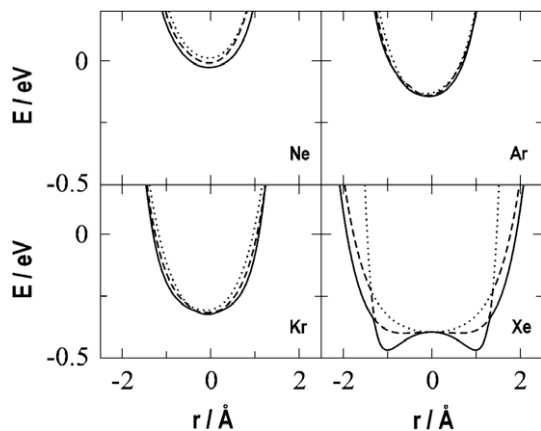


Fig. 2. Projection of the potential energy surfaces associated with the adiabatic levels correlated to the 3P_1 electronic excited state of the mercury embedded in rare gas matrices, in a plane that contains the impurity and six nearest neighbours. Solid line refers to adiabatic level 1, dashed line to adiabatic level 2 and points to adiabatic level 3.

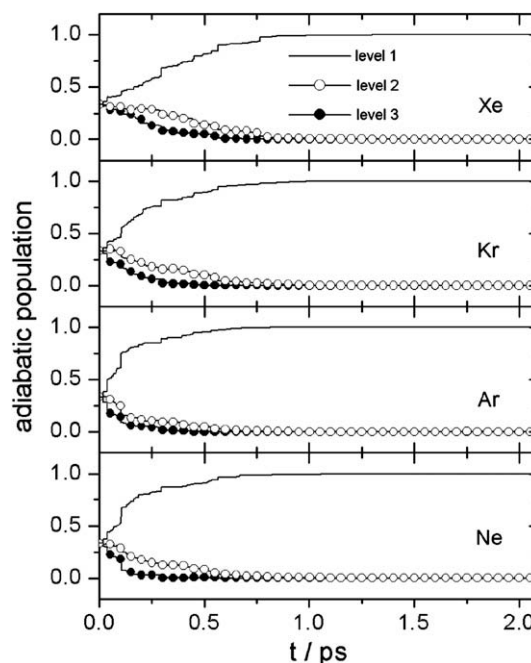


Fig. 3. Population of adiabatic levels as a function of time.

shrinkage of the matrix cage by $\sim 9\%$, $\sim 2\%$ and $\sim 2\%$ of the initial cage radius in Ne, Ar and Kr solids, respectively. These small changes are in line with the small reorganization energy reflected in the Stokes shifts. No coherence has been found in the dynamical response of these three matrices. These features can be seen in Fig. 4, where the evolution of the distance of the 12 nearest neighbours to the impurity is shown.

8. Structural dynamics in solid Xe

Fig. 5 shows a comparison of the radial distribution function of pure Xe and Xe/Hg doped solids at the ground and excited states. It can be seen that the substitution of a Xe atom by a Hg atom does not perturb the lattice significantly. This is in line with the comparable sizes of Hg and Xe and the fact that the Hg–Xe potential min-

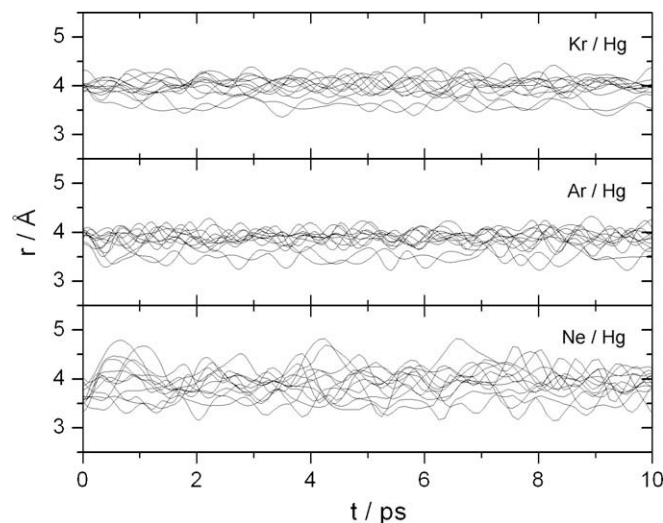


Fig. 4. Distance to the impurity of the 12 nearest neighbour atoms as a function of time.

imum is close to the Xe–Xe potential (see Table 1). A different situation is observed at the excited state, where a new peak appears at shorter distances than the one corresponding to the ground state first shell. Furthermore, the integrated area of the first two peaks in the excited state is the same as that of the first peak in the ground state RDF. The new peak corresponds to ~ 2 Xe atoms, suggesting that two atoms become closer to the Hg atom in the excited state, forming therefore a triatomic complex.

All the trajectories finally undergo Xe–Hg–Xe exciplet formation, but in two conformations: bent and linear. Furthermore, two different mechanisms, sequential and concerted, have been observed. Fig. 6 presents a set of five typical trajectories in distance. The trajectories amount to 29% (a), 7% (b), 14% (c), 48% (d), and 2% (e) and (f) of the total number of trajectories (300). In all the cases, the two Xe atoms have come close to the Hg atom in ~ 10 ps. Fig. 6a and b show the Hg–Xe distances for the Xe atoms in the first solvation shell as a function of time. It can be noticed that right from the beginning, two atoms move close to the impurity in a concerted way. In Fig. 6a these atoms come from a linear axis with the impurity, such that a linear Xe–Hg⁺–Xe complex is formed (the angle Xe–Hg⁺–Xe remains oscillating near 180° as is shown in Fig. 7). The two Xe atoms oscillate at nearly the same frequency but out of phase. The oscillations are described with a slight damping over the time scale of 10 ps. The Hg atom remains at the centre of the cavity and the rest of the Xe neighbours keep their distances to the impurity in time. In Fig. 6b the two Xe atoms are not in line with the Hg atom, such that a non-linear complex is created (the angle Xe–Hg⁺–Xe remains oscillating near 150° as is shown in Fig. 7). Their oscillations are out of phase describing a clear antisymmetric stretch mode. A huge dispersion is observed in the distances between the twelve Xe atoms of the first solvation shell and the Hg atom, as a function of time. This is a consequence of the displacement of the Hg atom from its initial position at the centre of the cavity.

A sequential mechanism is also observed during the formation of the excited Xe–Hg⁺–Xe complex. This mechanism can be shown in Fig. 6c and d. The first Xe atom comes close to the impurity at very short times and it oscillates at a frequency of ~ 55 cm⁻¹. After 2 or 3 ps, the second Xe atom approaches the mercury and oscillates around the same frequency, but out of phase in an antisymmetric stretch mode. The sequential mechanism in the exciplet formation, also leads to linear (Fig. 6c) and non-linear (Fig. 6d) complexes (see also Fig. 7). Once again the impurity remains in the centre of the cavity for linear complexes and moves out of the centre in the non-linear triatomic complexes.

At this point it is interesting to mention that atomic exchange has been observed during the formation and stabilization of the complexes. This process is exemplified in Fig. 6e and f and it has been observed in the 10% of trajectories.

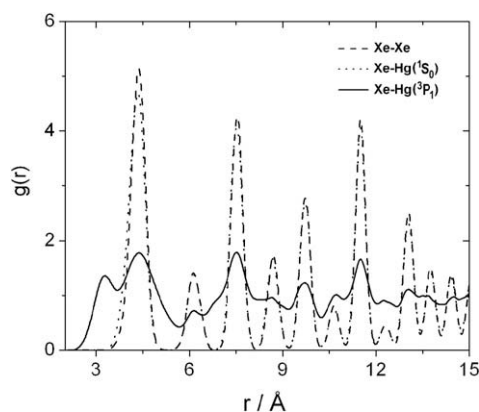


Fig. 5. Stationary pair distribution functions $g(r)$ in Xe and Xe/Hg matrices.

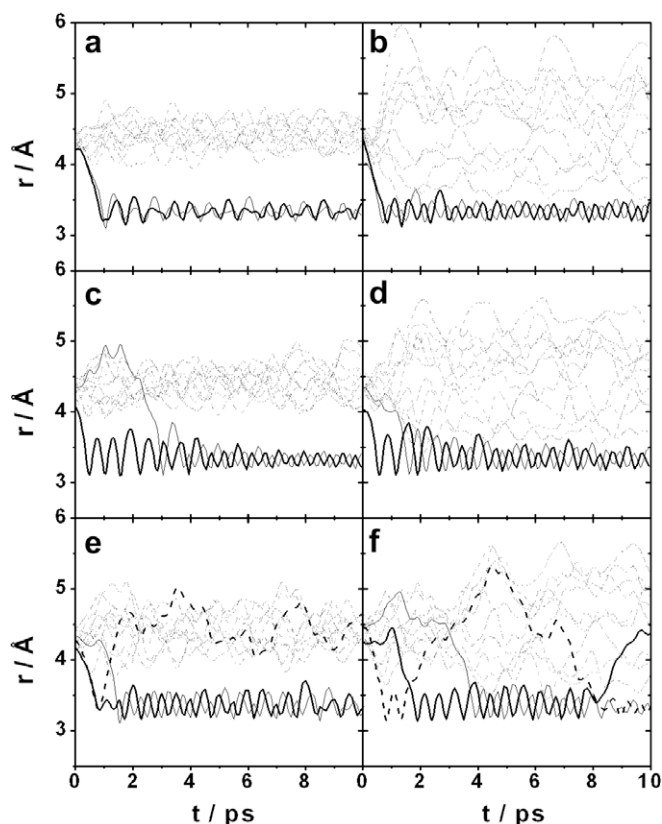


Fig. 6. Distance to the impurity of the 12 nearest neighbour atoms as a function of time. Triatomic complex formation found in five typical trajectories. In figure are represented the cases: (a) concerted and linear, (b) concerted and non-linear, (c) sequential and linear, (d) sequential and non-linear, (e) and (f) atomic exchange.

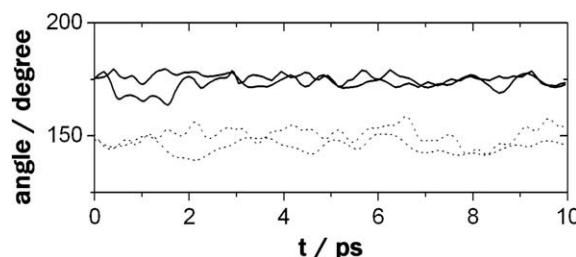


Fig. 7. Angle Xe–Hg–Xe in the complex as a function of time. In solid lines are presented the linear cases (a) and (c), and in dotted lines are shown the cases (b) and (d) shown in Fig. 6.

In order to analyze the relation observed between non-linear complex formation, and the displacement of impurity from the centre of the cavity, two different kinds of simulations were performed. On one hand, the simulations were carried out at classical 4 K (without quantum thermal correction) in order to constraint the zero phonon amplitude of the mercury. On the other hand, the simulations were performed increasing 10 times the impurity mass. Both procedures were designed to preserve the mercury atom at the centre of the cavity. As a result, all the trajectories calculated with these schemes lead to the formation of linear triatomic complex. Therefore, these results pointed at a direct relationship between the displacement of the Hg atom out of the centre of the cavity and the formation of non-linear triatomic complex.

Fig. 8 shows the Fourier transforms corresponding to the distances and angles depicted in Figs. 6 and 7. The Fig. 8a and b rep-

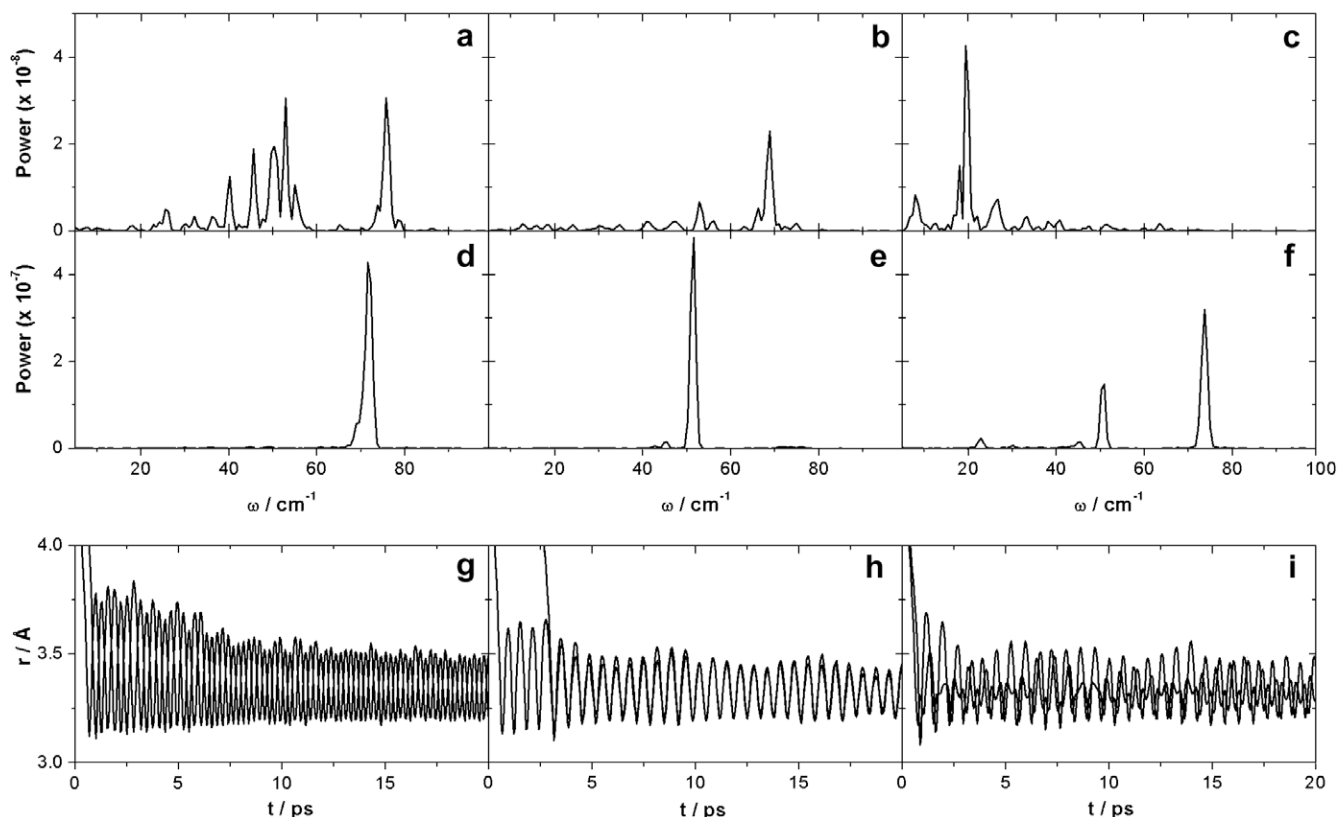


Fig. 8. Mean frequency contributions obtained from Fourier transform of distances and angles. In figure are presented the Fourier transform of: (a) Xe–Hg distance in linear complex at 32 K, (b) Xe–Hg distance in non-linear complex at 32 K, (c) Xe–Hg–Xe angle in a non-linear complex. (d), (e), and (f) Xe–Hg distance in the complex at 4 K. In (g), (h) and (i) are shown distances Xe–Hg in the complex as a function of time at 4 K, correlated to (d), (e) and (f), respectively.

represent the Fourier transform of the Xe–Hg distance during the complex described by Fig. 6a and b, respectively. The main peaks at ~ 53 cm⁻¹ and ~ 75 cm⁻¹ correspond to frequencies higher than the corresponding to the Debye frequency of the Xe crystal (46 cm⁻¹) and they were found in all the complexes. According to the comparative analysis of the Fig. 8d–h, these frequencies correspond to the symmetric and antisymmetric stretch modes of the Xe–Hg–Xe complex, respectively. The evolution of distances Xe–Hg in the majority of complexes present a pattern (Fig. 8i) defined by the superposition of the two stretch modes (Fig. 8f). Finally, the Fourier transform of the Xe–Hg–Xe angle (Fig. 7) is displayed in Fig. 8c. The peak at ~ 20 cm⁻¹ indicates that the complex is coupled with the matrix trough its bend mode and it appears in all the trajectories.

The fraction of f trajectories that leads to the formation of the linear complex depends on the initially excited adiabatic state. These values were 53%, 35%, and 21% for simulations performed by initially populating the adiabatic levels 1, 2 and 3, respectively. Finally, at 32 K, in 37% of all trajectories were found linear triatomic complexes. On one hand, the formation of the non-linear complexes is favoured by geometrical disposition of the nearest neighbours Xe atoms to the impurity in the f.c.c. crystal (12 linear vs. 54 non-linear). On the other hand, the formation of linear complexes is energetically preferred by about ~ 700 cm⁻¹. In Fig. 9 we represent the emission band associated to the electronic transition $^3P_1 \rightarrow ^1S_0$ of the mercury atom in Xe matrices. The contributions of both types of complexes, i.e. linear and non-linear triatomic Xe–Hg⁺–Xe complexes, are also indicated. Therefore, this result explains the broadening in the emission band previously reported in the experiments [16,17,19].

The presence of diatomic complexes Hg–Xe was also observed during our simulations (Fig. 10). The diatomic complex is the first

step in the sequential mechanism for the triatomic complex formation. Nevertheless, only the triatomic complexes were observed after the first ~ 10 ps of the dynamics after the photoexcitation. The formation of diatomic Hg⁺–Xe structures increases at the beginning of the simulations and reaches a maximum value at 500–1000 fs after the photoexcitation. After that time, the population of diatomic complexes decreases smoothly to zero. At the same time, an increase in the number of Xe–Hg⁺–Xe complexes is observed. The non-linear complex formation was shown to be fas-

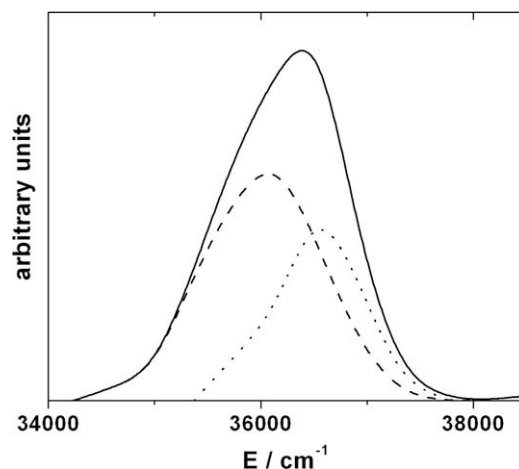


Fig. 9. Emission band $^3P_1 \rightarrow ^1S_0$ reported in Xe/Hg crystals upon photoexcitation of mercury atom. The contribution of linear excited complexes is represented with points, the contribution of non-linear triatomic molecules is shown with dashed line, and total profile is presented with solid line in figure.

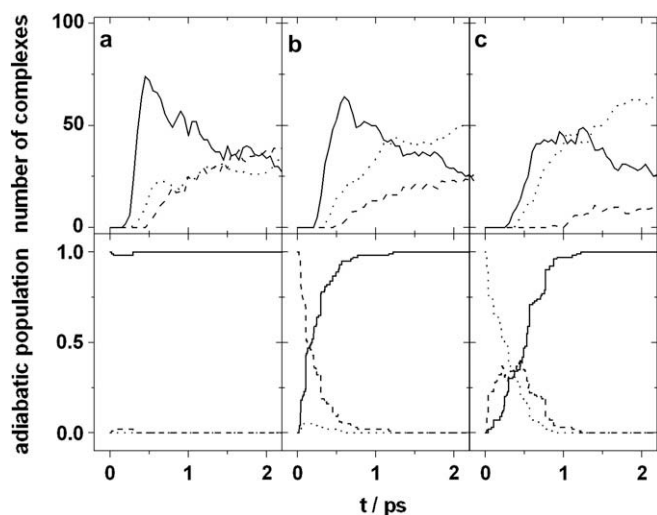


Fig. 10. On top is presented the number of excited complexes as a function of time. With solid lines are shown the diatomic complexes, with dashed lines the linear triatomic complexes, and with points the non-linear triatomic molecules. On bottom is shown temporal behaviour of the population of adiabatic levels. With solid lines are presented adiabatic level 1, with dashed lines adiabatic levels 2 and with dots adiabatic levels 3.

ter than the corresponding formation of linear complexes. As can be seen in Fig. 10, the population of the linear complexes becomes important when the adiabatic level 1 reaches a population close to 100% (after 500 or 1000 fs), in line with the maximum of population for diatomic species.

9. Conclusions

The results obtained for absorption bands, emission bands and Stokes shifts related to the electronic transitions $^1S_0 \leftrightarrow ^3P_1$ of atomic mercury in rare gas matrices are qualitatively in good agreement with available experimental data. This point allows to interpolate the evolution of the system between the two stationary states (1S_0 ground and 3P_1 excited electronic states of the mercury). The triplet structure of the absorption band is related to the breakdown of the 3P_1 degeneracy, in contrast to the assumption of a dynamical Jahn Teller effect. Nevertheless, the single structure of the emission band is related to the 100% populated adiabatic level, corresponding to the level with the less energy among those that correlates asymptotically with the 3P_1 electronic excited state of atomic mercury.

In the case of xenon matrices doped with atomic mercury, the formation of $HgXe_2$ takes place in less than 10 ps after photoexcitation. However, during the first 500–1000 fs the dynamics is dominated by the $HgXe$ diatomic formation, as a first step on the formation of triatomic molecules in a sequential framework. This result reinforces the predominance of triatomic complex formation in a sequential mechanism (62%) over the concerted mechanism (36%).

The analysis of the final configurations achieved by our simulations indicates the formation of two isomers of the triatomic complex $Xe-Hg^+-Xe$. The presence of bent molecules (63%) predominates over the formation of linear complexes (37%). The thermal fluctuations of the mercury atom inside the rare gas

matrix were found to be responsible for the formation of the bent complexes. Two vibrational modes of the triatomic complexes have been identified: the symmetric stretch mode at 53 cm^{-1} , and the antisymmetric stretch mode at 75 cm^{-1} . These modes are not coupled to the matrix as their frequency values are greater than Debye frequency for Xe matrices. The energy relaxation mechanism of triatomic molecule can take place through its bent mode at 20 cm^{-1} , that can be coupled to the matrix modes.

The asymmetry of the emission band experimentally observed in Xe matrices can be attributed to the overlap of two emission bands, with different intensities, associated to the formation of the bent and the linear $Xe-Hg^+-Xe$ complexes, respectively.

The methodology applied in this work can be generalized to describe the formation of self-trapped excitons (atomic and molecular) in pure rare gas solids. Besides, the study of the dynamical response of Ar solids doped with atomic Hg and Xe atoms due the photoexcitation of Hg to its 3P_1 electronic excited state can be performed. Further studies on these topics are in progress.

Acknowledgements

We would like to acknowledge fruitful discussions with Prof. Majed Chergui, Prof. Julián Echave and Prof. Kenneth Janda. G. Rojas-Lorenzo acknowledges the Ministerio de Ciencia e Innovación (Spain) for the Project SB2006-0011.

References

- [1] T. Shibata, S. Iwai, T. Tokizaki, et al., *Phys. Rev. B* 49 (1994) 13255.
- [2] R. Scholz, M. Schreiber, F. Bassani, et al., *Phys. Rev. B* 56 (1997) 1179.
- [3] M. Nisoli, S. DeSilvestri, O. Svelto, et al., *Phys. Rev. Lett.* 77 (1996) 3463.
- [4] A. Lushchik, M. Kirm, C. Lushchik, et al., *J. Lumin.* 87–89 (2000) 232.
- [5] I.N. Ogorodnikov, V.A. Pustovarov, A.V. Kruzhakov, et al., *Phys. Solid State* 42 (2000) 464.
- [6] V.A. Apkarian, N. Schwentner, *Chem. Rev.* 99 (1999) 1481.
- [7] K. Bammel, P. Dietrich, N. Schwentner, *J. Chem. Phys.* 111 (1999) 2123.
- [8] A.N. Ogurtsov, E.V. Savchenko, E. Sombrowski, et al., *Low Temp. Phys.* 29 (2003) 858.
- [9] C. Jeannin, M.T. Porrella-Oberli, S. Jimenez, et al., *Chem. Phys. Lett.* 316 (2000) 51.
- [10] G. Lanzani, S.V. Frolov, P.A. Lane, et al., *Phys. Rev. Lett.* 79 (1997) 3066.
- [11] A. Sugita, T. Saito, H. Kano, et al., *Phys. Rev. Lett.* 86 (2001) 2158.
- [12] A. Sugita, M. Yamashita, T. Kobayashi, *J. Chem. Phys.* 114 (2001) 2369.
- [13] L. Skuja, *J. Non-Cryst. Solids* 239 (1998) 16.
- [14] M. Leone, S. Agnello, R. Boscaino, et al., in: H.S. Nalwa (Ed.), *Silicon-based Materials and Devices*, vol. 2, Academic Press, 2001, p. 2.
- [15] S. Agnello, R. Boscaino, M. Cannas, et al., *Phys. Rev. B* 68 (2003).
- [16] C. Crepin, A. Tramer, *J. Chem. Phys.* 97 (1992) 4772.
- [17] J. Helbing, M. Chergui, A. Haydar, *J. Chem. Phys.* 113 (2000) 3621.
- [18] J. Helbing, A. Haydar, M. Chergui, *Chem. Phys. Lett.* 310 (1999) 43.
- [19] M.A. Collier, J.G. McCaffrey, *J. Chem. Phys.* 119 (2003) 11878; M.A. Collier, J.G. McCaffrey, *J. Chem. Phys.* 119 (2003) 11888.
- [20] J.C. Tully, *Faraday Discuss.* 407 (1998).
- [21] D. Kohen, F.H. Stillinger, J.C. Tully, *J. Chem. Phys.* 109 (1998) 4713.
- [22] K. Yamanouchi, S. Isogai, M. Okunishi, et al., *J. Chem. Phys.* 88 (1988) 205.
- [23] M. Okunishi, H. Kanazawa, K. Yamanouchi, et al., *J. Chem. Phys.* 93 (1990) 7526.
- [24] K. Yamanouchi, J. Fukuyama, H. Horiguchi, et al., *J. Chem. Phys.* 85 (1986) 1806.
- [25] N.W. Ashcroft, N.D. Mermin, *Solid State Physics*, Holt, New York, 1976.
- [26] J. Zuniga, A. Bastida, A. Requena, et al., *J. Chem. Phys.* 98 (1993) 1007.
- [27] G. Rojas-Lorenzo, J. Rubayo-Soneira, M. Chergui, et al., *J. Phys. Chem. A* 107 (2003) 8225.
- [28] J.P. Bergsma, P.H. Berens, K.R. Wilson, et al., *J. Phys. Chem.* 88 (1984) 612; L. Uranga-Piña, A. Martínez-Mesa, et al., *Chem. Phys. Lett.* 429 (2006) 450.
- [29] R.L. Mowery, et al., *J. Chem. Phys.* 70 (1979) 3920.
- [30] P.A. Lund et al., *J. Phys. Chem.* 88 (1984) 31.
- [31] K.J. Zeringue et al., *J. Chem. Phys.* 78 (1983) 2231.